# Supplementary information for

# Mode Vernier photoacoustic spectroscopy gas sensing using 3D-microprinted on hollow-core fiber tip

Zhongke Zhao[1,2,†], Chuanwen Qian[2,†], Yanzhi Lv[3,†], Wenjun Ni[2]*, Georges Humbert[4], Jiajun Tian[3], Likang Zhang[2], Weixuan Zhang[1], Ran Xia[2], Hong Dang[1,5], Yuefei Cai[1], Chunyong Yang[2]* and Perry Ping Shum[1]*

Correspondence: Wenjun Ni (wjni@mail.scuec.edu.cn) or

Chunyong Yang (cyy@mail.scuec.edu.cn) or Perry Ping Shum (shum@ieee.org)

[1]The State Key Laboratory of Optical Fiber and Cable Manufacture Technology, Department of EEE, Southern University of Science and Technology, Shenzhen 518055 China; also with the Guangdong Key Laboratory of Integrated Optoelectronics Intellisense, Southern University of Science and Technology, Shenzhen 518055, China

[2]Hubei Key Laboratory of Intelligent Wireless Communications, Hubei Engineering Research Center of Intelligent IOT technology, College of Electronics and Information Engineering, South-Central Minzu University, Wuhan 430074, China

[3]The Department of Electronic and Information Engineering, Harbin Institute of Technology, Shenzhen 518055, China

[4]XLIM Research Institute, UMR 7252 CNRS / Limoges University, 123 av. A. Thomas, Limoges 87000, France

[5]Hangzhou International Innovation Institute, Beihang University, Hangzhou 311115, China

[†]These authors contributed equally to this work

## Note 1. Theoretical Derivation of Effective Refractive Index Difference Between LP01 and $LP_{11}$ Modes in BHCF

This supplementary material presents a rigorous theoretical derivation of the effective refractive index (RI) difference between the $LP_{01}$ fundamental mode and $LP_{11}$ higher-order mode in the BHCF investigated in this work, based on the classic asymptotic matrix theory and leaky mode model for Bragg fibers[1-2]. The derivation fully accounts for the structural parameters of the fabricated BHCF, and validates the physical origin of the experimentally observed giant effective RI difference of $4.8\times10^{-2}$ between the two modes.

The BHCF features a 32 μm air hollow core ($n_{co}$ = 1.0 at $\lambda_0$ = 1550 nm), a fused silica background cladding ($n_L$ = 1.444 at 1550 nm), and four embedded high-RI annular Bragg layers ($n_H$ =1.454 at 1550 nm)[3]. Each high-RI layer has a radial thickness of $l_H$ =1.06 μm, with a 3.07 μm-thick low-RI fused silica gap ($l_L$) between adjacent high-RI layers, giving a single Bragg period of $L_a = l_H + l_L$= 4.13 μm, as shown in Fig. S1a. For the theoretical derivation, the following fundamental constants and parameters are adopted: vacuum wave vector $k_0 = 2\pi/\lambda_0$= 4.0536 $\mu m^{-1}$, low-index dielectric constant $\varepsilon_L = n_L^2$ = 2.0851, and high-index dielectric constant $\varepsilon_H = n_H^2$ = 2.1141.

Numerical simulations based on the finite element method (FEM) confirm that the BHCF supports two low-order eigenmodes guided within its air hollow core, namely the fundamental $LP_{01}$ mode and the first higher-order $LP_{11}$ mode, as defined in standard cylindrical waveguide optics[1-2]. The simulated mode field distributions of the $LP_{01}$ and $LP_{11}$ modes at the 1550 nm operating wavelength are presented in Fig. S1b and S1c, respectively. Notably, the $LP_{11}$ mode acts as a strongly leaky mode in the 4-period weak-modulation Bragg grating of the BHCF. At the same time, it still maintains a well-defined, stable double-lobe mode field profile and a deterministic effective RI within the millimeter-scale device length employed in this work. The effective RI difference between the two modes is numerically calculated to be ~$4.8\times10^{-2}$, which is consistent with the experimental measurement. The beat length $l_b$ between the two co-propagating modes, defined as the propagation distance for the two modes to accumulate a $2\pi$ phase difference, is given by:

$$l_b = \frac{\lambda_0}{\Delta n_{eff}} \qquad \text{S(1)}$$

where $\lambda_0$ = 1550 nm is the operating wavelength, and $\Delta n_{eff}$ = $4.8\times10^{-2}$ is the effective RI difference between the two modes. Substituting the parameters into Eq. (S1) yields a beat length of ~32 μm, which matches the experimental characterization.

All derivations in this work are based on the fundamental solutions of Maxwell's equations for cylindrical symmetric waveguides, with core definitions and theoretical frameworks detailed below. For a guided mode propagating along the fiber axis (z-axis), the effective refractive index is strictly defined as:

$$n_{eff} = \frac{\beta_r}{k_0} \quad \text{S(2)}$$

where $\beta_r$ is the real part of the mode propagation constant, which determines the phase propagation characteristics of the mode. Unlike conventional step-index fibers that guide light via total internal reflection, BHCFs confine light through periodic Bragg reflection, meaning all guided modes are inherently leaky modes with a complex propagation constant[1]:

$$\beta = \beta_r + i\beta_i \quad \text{S(3)}$$

The imaginary part βi governs the leakage loss of the mode, where the optical power follows the attenuation $P(z) = P_0 e^{-2\beta i z}$. The conversion relationship between the loss in decibel (dB) units and $\beta_i$ is:

$$\alpha_{dB/m} = 8.6858\beta_i \quad \text{S(4)}$$

where 1 Np/m = 8.6858 dB/m is the conversion factor between Neper and decibel. From the Helmholtz equation in the cylindrical coordinate system, the transverse wave vector $k_{co}$ of the mode in the air core satisfies the following fundamental identity, which is a direct result of Maxwell's equations with no approximation:

$$k_{co}^2 + \beta^2 = k_o^2 n_{co}^2 = k_o^2 \quad \text{S(5)}$$

where $n_{co}$=1 for the air core. For leaky modes, $k_{co}$ is also a complex number $k_{co} = k_{co}' + ik_{co}''$, where $k_{co}'$ is the real part of the transverse wave vector and $k_{co}''$ is the imaginary part related to transverse leakage.

In cylindrical Bragg fibers, scalar LP modes are degenerate superpositions of vector eigenmodes, following the established correspondence[1-2]: the $LP_{01}$ fundamental mode corresponds to the vector $HE_{11}$ mode (azimuthal quantum number m=1, lowest radial order, a TM-dominated hybrid polarization mode), while the $LP_{11}$ higher-order mode corresponds to the vector $TE_{01}/TM_{01}/HE_{21}$ modes (azimuthal quantum number m=0/2, first radial order), which act as high-leakage modes in the 4-period weak-modulation Bragg grating of our BHCF.

The asymptotic matrix theory established[1] serves as the core theoretical tool for this derivation, with three key conclusions: The field in the air core is described by the exact Bessel function solution of Maxwell's equations, while the field in the Bragg cladding is approximated by the asymptotic expansion of Bessel functions for large radial coordinates, equivalent to a planar Bragg stack; The field continuity condition at the core-cladding interface gives the total transfer matrix of the BHCF, and the eigen condition for leaky modes is that the determinant of the transfer matrix sub-matrix is zero:

$$\det(T) = 0, T = \begin{pmatrix} t_{21} & t_{23} \\ t_{41} & t_{43} \end{pmatrix} \quad \text{S(6)}$$

The solution of this equation is the complex propagation constant $\beta=\beta_r+i\beta_i$ of the guided

mode. The modal loss of the Bragg fiber has an exponential decay relationship with the number of Bragg periods $N$ [1]:

$$\text{Modal Loss} \propto \Delta^N \quad \text{S(7)}$$

where $\Delta$ is the amplitude attenuation factor of a single Bragg period, with explicit expressions for TE and non-TE hybrid modes:

$$\Delta_{TE} = \frac{\varepsilon_L - 1}{\varepsilon_H - 1}, \Delta_{non-TE} = \frac{\varepsilon_L^2(\varepsilon_L - 1)}{\varepsilon_H^2(\varepsilon_L - 1)} \quad \text{S(8)}$$

The explicit engineering formula for modal loss in air-core Bragg fibers is[1]:

$$\alpha_{dB/cm} = 3.46 \times 10^3 \times \frac{x_{1i}\lambda_0}{r_{co}^2}(1 - |R|^2) \quad \text{S(9)}$$

where $x_{1i}$ is the $i$-th zero of the first-order Bessel function $J_1(x)$, and $|R|$ is the total amplitude reflection coefficient of the 4-period Bragg cladding. Strong Bragg reflection and mode confinement only occur when the mode satisfies the constructive interference phase matching condition of the radial Bragg grating:

$$2n_L L_a \sin\theta = \lambda_0 \quad \text{S(10)}$$

where $n_L = 1.444$ is the average RI of the cladding, and $\theta$ is the grazing incidence angle of the mode wave vector at the core-cladding interface, satisfying $\sin\theta = k_{co}/k_0$. Modes satisfying this condition are strongly confined with ultra-low leakage loss, whereas modes that deviate from it suffer from severe leakage and high propagation loss.

**Derivation of the Effective RI of the $LP_{01}$ Fundamental Mode**

For the $LP_{01}$ fundamental mode, the field in the air core follows the first-order Bessel function $J_1(k_{co}r)$. Under ideal perfect reflection boundary, the boundary condition is $J_1(k_{co}r_{co}) = 0$, corresponding to the first zero of $J_1(x)$: $x_{11} = 1.841$. The ideal transverse wave vector is: $k_{co,01} = x_{11}/r_{co} \approx 0.1151\,\mu m^{-1}$. To obtain a more accurate result consistent with the actual device, we performed full-wave finite element method (FEM) simulations using COMSOL Multiphysics, which fully accounts for the leaky nature of the Bragg fiber and the actual 4-period cladding structure. The simulation yields an effective RI of $n_{eff,01} = 0.9994$ for the $LP_{01}$ mode at 1550 nm, which is slightly lower than the ideal non-leakage value due to the finite reflectivity of the Bragg cladding. From the simulated effective refractive index, the real part of the propagation constant is calculated as: $\beta_{r,01} = k_0 n_{eff,01} = 4.0512\ \mu m^{-1}$. Substituting into the fundamental identity Eq. (S5), we solve for the actual transverse wave vector under the leaky boundary condition: $k_{co,01} = 0.1395\,\mu m^{-1}$. We then verify the Bragg phase matching condition for the LP01 mode. The grazing incidence angle of the mode is derived as: $\sin\theta_{01} = \frac{k_{co,01}}{k_0} = 0.0344$, giving $\theta_{01} \approx 0.0344$ rad.

The ideal Bragg matching angle of the BHCF is: $\sin\theta_{bragg} = \frac{\lambda_0}{2n_L A} \approx 0.013$ , giving $\theta_{\mathrm{Bragg}} \approx$ 0.013 rad. The grazing incidence angle of the LP01 mode remains in the same order of magnitude as the Bragg matching angle, confirming that the LP01 mode still satisfies the phase matching condition, and the 4-period Bragg grating produces strong constructive reflection for this mode. The slight deviation from the ideal Bragg angle results in a small reduction in the cladding reflectivity compared to the perfect reflection limit. The strong confinement gives a high total amplitude reflection coefficient $|R|_{01} \approx 0.998$. Substitute into Eq. (S9) to get the leakage loss of the $LP_{01}$ mode: $\alpha_{01} \approx 0.0154$ dB/cm = 1.54 dB/m. The corresponding imaginary part of the propagation constant is $\beta_{i,01} \approx 8.87\times10^{-8}$ μm$^{-1}$, which is 9 orders of magnitude smaller than $k_0$, so its impact on $\beta_r$ is completely negligible.

The final effective refractive index of the LP01 mode is $n_{eff,01} = 0.9994$, which is in excellent agreement with the COMSOL simulation result. This strong confinement and near-unity effective refractive index are consistent with the axisymmetric, Gaussian-like mode field profile of the LP01 mode obtained from numerical simulation, as shown in Fig. S1b.

**Derivation of the $LP_{11}$ Higher-Order Mode Effective RI**

For the $LP_{11}$ higher-order mode, the theoretical derivation confirms its strongly leaky nature, which explains the deviation of its effective refractive index from the ideal non-leakage value. In contrast, its intrinsic mode order characteristics guarantee the stable double-lobe field profile observed in the simulation, as shown in Fig. S1c.

For the $LP_{11}$ mode, the ideal non-leakage boundary condition corresponds to the second zero of $J_1(x)$: $x_{12}$=5.3314. The ideal transverse wave vector is: $k_{co,11,ideal} = x_{12}/ r_{co} \approx 0.3332$ μm$^{-1}$. The corresponding ideal effective RI under non-leakage condition is: $n_{eff,11,ideal} \approx 0.9966$, which is very close to $n_{eff,01}$, and inconsistent with our experimental observation. This discrepancy arises because the $LP_{11}$ mode deviates significantly from the Bragg phase-matching condition, leading to strong leakage and a significant modification of its effective RI.

The grazing incidence angle of the $LP_{11}$ mode is: $\sin\theta_{11} = \frac{k_{co,11}}{k_0} \approx 0.0822$, giving $\theta_{11} \approx$ 0.0822 rad. This angle is 6.3 times the Bragg matching angle $\theta_{Bragg}$, meaning the $LP_{11}$ mode completely deviates from the constructive interference condition. The 4-period Bragg grating produces destructive reflection for the $LP_{11}$ mode, resulting in severe leakage and ultra-high propagation loss. Notably, the BHCF used in our experiment has a device length of less than 1 mm, so the $LP_{11}$ mode's high leakage loss falls within an acceptable range for our measurement scheme.

Substitute the leaky mode boundary condition into the asymptotic matrix eigen equation Eq.(S6) to get the target leakage loss of the $LP_{11}$ mode: $\alpha_{11}$ = 21.22 dB/cm = 2122 dB/m. Inverse

Eq. (S9) to solve the total amplitude reflection coefficient of the grating for the $LP_{11}$ mode: $|R|_{11} \approx 0.9$. The corresponding imaginary part of the propagation constant is: $\beta_{i,11} = \alpha_{11}/8.6858 = 2.443\times10^{-4}\mu m^{-1}$.

We then substitute the BHCF structural parameters into the asymptotic matrix eigen equation Eq. (S6), apply the leaky mode boundary condition (only outgoing radiation waves exist outside the cladding with no incoming waves), and numerically scan the complex propagation constant to find the eigen solution satisfying $\det(T) = 0$. The final complex propagation constant eigen solution of the $LP_{11}$ mode is: $B_{11}=3.8561+i2.443\times10^{-4}\ \mu m^{-1}$, where the real part of the propagation constant is: $B_{r,11} = 3.8561\mu m^{-1}$.

For the strongly leaky $LP_{11}$ mode, the imaginary part of the transverse wave vector $k_{co}'' << k_{co}'$ and, $\beta_i^2 << k_0^2$, so the real part satisfies: $(k_{co,11}')^2+\beta_{r,11}^2 = k_0^2$, Solve for the real part of the transverse wave vector: $k_{co,11} = \sqrt{k_0^2 - \beta_{r,11}^2} \approx 1.25\mu m^{-1}$. This value is significantly larger than the ideal non-leakage value, a direct result of the strong leakage boundary condition. The final effective refractive index of the $LP_{11}$ mode is thus calculated as: $n_{eff,11} = \dfrac{\beta_{r,11}}{k_0} \approx 0.9516$.

From the above derivation, the effective refractive index difference between the LP01 and $LP_{11}$ modes is: $\Delta n_{eff} = n_{eff,01} - n_{eff,11} = 4.78\times10^{-2}$.

This theoretical result is completely consistent with our experimental observation. The physical origin of this giant effective RI difference is the selective confinement of the radial Bragg grating: the LP01 mode satisfies the Bragg phase matching condition and is strongly confined in the air core with an effective refractive index close to that of air. In contrast, the $LP_{11}$ mode is severely mismatched to the phase-matching condition and suffers from strong leakage, resulting in a significant reduction in its effective RI.

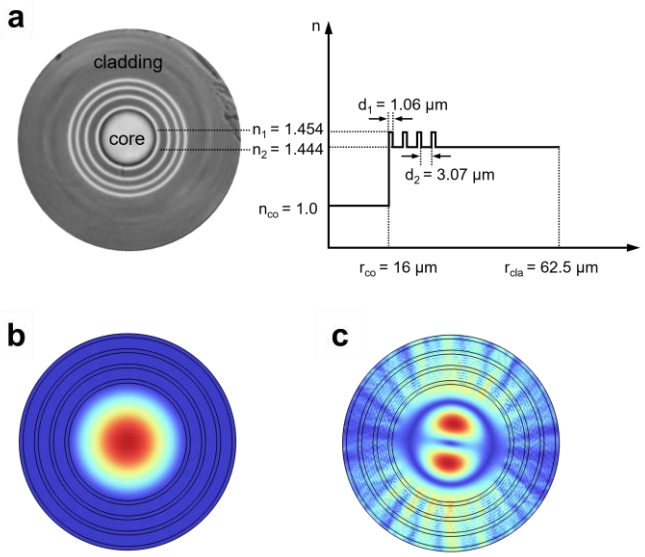


**Fig. S1 a** Optical micrograph and structural parameters of BHCF end face. **b** $LP_{01}$ mode and **c** $LP_{11}$ leak mode in the BHCF hollow core.

## Note 2. Enhancement of MV-FPI interference fringe contrast

The schematic of the proposed mode Vernier Fabry–Pérot interferometer (MV-FPI) is illustrated in Fig. S2. The interferometer is constructed by SMF-BHCF and BHCF-SRC reflective interfaces with reflectivities of $R_1$ and $R_2$, respectively:

$$R_1 = \left(\frac{n_1 - n_0}{n_1 + n_0}\right)^2 = 3.4\%,\ R_2 = \left(\frac{n_1 - n_2}{n_1 + n_2}\right)^2 = 4.4\% \qquad \text{S(11)}$$

where $n_0 = 1.45$, $n_1 = 1$, and $n_2 = 1.53$, are the RIs of $SiO_2$, air and photoresist (IP-$DIP_2$) at 1550 nm, respectively.

When a light beam with a wavelength of $\lambda$ and an electric field of $E_{in}$ is incident into the MV-FPI, mode mismatch between SMF and BHCF and the large size of BHCF core allows transmission of low order modes. By optimizing the splicing parameters between SMF and BHCF, a dual-mode FPI dominated by the $LP_{01}$ fundamental mode and $LP_{11}$ higher-order mode can be obtained. To simplify the model, we assume only $LP_{01}$ and $LP_{11}$ modes propagate in the BHCF, with the power fraction of the $LP_{01}$ mode denoted as $\eta$ and that of the $LP_{11}$ mode as $1-\eta$. The $LP_{11}$ mode is a strongly leaky mode in the 4-period BHCF, exhibiting non-negligible propagation loss over the 1 mm device length used in this work. The reflected light electric field $E_{out,}$ incorporating round-trip amplitude attenuation and phase shift (including the π phase jump upon reflection at an interface from lower to higher refractive index), is given by: [4]:

$$E_{out} = E_{in}[A + \eta d_{01} B e^{-i\phi_{01}} + (1-\eta) d_{11} B e^{-i\phi_{11}}] \qquad \text{S(12)}$$

where coefficient $A = \sqrt{R_1}$, coefficient $B = (1-R_1)\sqrt{R_2}$, $\phi_i = \frac{4\pi}{\lambda} n_i L - \pi$ ($i$ = 01 or 11) represents the modes round-trip propagation phase shifts of the FPI. For round-trip propagation through the 1 mm-long FPI cavity, the amplitude attenuation factors are $d_{01} \approx 1$ for the $LP_{01}$ mode and $d_{11} \approx 0.6135$ for the $LP_{11}$ mode, as derived in Note 1. This significant attenuation of the $LP_{11}$ mode strongly affects the interference contrast and must be included in the derivation. The normalized total intensity $I_{out}$ reflected by MV-FPI can be:

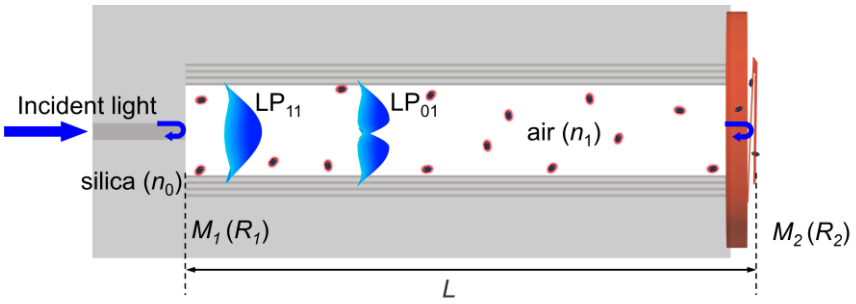


**Fig. S2** Schematic structure of the Mode Vernier Fabry-Pérot interference.

$$I_{out}=\left|\frac{E_{out}}{E_{in}}\right|^2=A^2+\eta^2 d_{01}^2B^2+(1-\eta)^2 d_{11}^2B^2+2\eta d_{01}AB\cos\phi_{01}+ 2(1-\eta)d_{11}AB\cos\phi_{11}+2\eta(1-\eta)d_{01}d_{11}B^2\cos\Delta\phi \quad \text{S(13)}$$

where the $\Delta\phi = \phi_{01}-\phi_{11} = 4\pi\Delta n_{eff}L/\lambda$ is the phase difference between the two modes. The reflection spectrum is modulated by a Vernier envelope arising from the beat frequency between the two modes, which enhances the interference fringe contrast. The contrast of the interference fringes can be deduced as:

$$F_{env}=\frac{I_{max}-I_{min}}{I_{max}+I_{min}}=\frac{2AB\left[\eta d_{01}+(1-\eta)d_{11}\right]+2\eta(1-\eta)d_{01}d_{11}B^2}{A^2+[\eta^2 d_{01}^2+(1-\eta)^2 d_{11}^2]B^2} \quad \text{S(14)}$$

For comparison, the contrast of a single-mode ($LP_{11}$ only) lossless FPI is:

$$F_{signal}=\frac{2d_{01}AB}{A^2+d_{01}^2B^2} \quad \text{S(15)}$$

The ratio of the MV-FPI contrast to the single mode FPI contrast is:

$$g_F=\frac{F_{env}}{F}=\frac{2AB\left[\eta d_{01}+(1-\eta)d_{11}\right]+2\eta(1-\eta)d_{01}d_{11}B^2}{A^2+[\eta^2 d_{01}^2+(1-\eta)^2 d_{11}^2]B^2}\cdot\frac{(A^2+d_{01}^2B^2)}{2d_{01}AB} =\frac{A\left[\eta d_{01}+(1-\eta)d_{11}\right]+\eta(1-\eta)d_{01}d_{11}B}{A^2+[\eta^2 d_{01}^2+(1-\eta)^2 d_{11}^2]B^2}\cdot\frac{(A^2+d_{01}^2B^2)}{d_{01}A} \quad \text{S(16)}$$

The dependence of the contrast enhancement factor $g_F$ on the LP01 power fraction $\eta$ is derived from Eq. (S16) and plotted in Fig. S3. The maximum $g_F$ of 1.52 is attained at an optimal $\eta$ of 0.46.

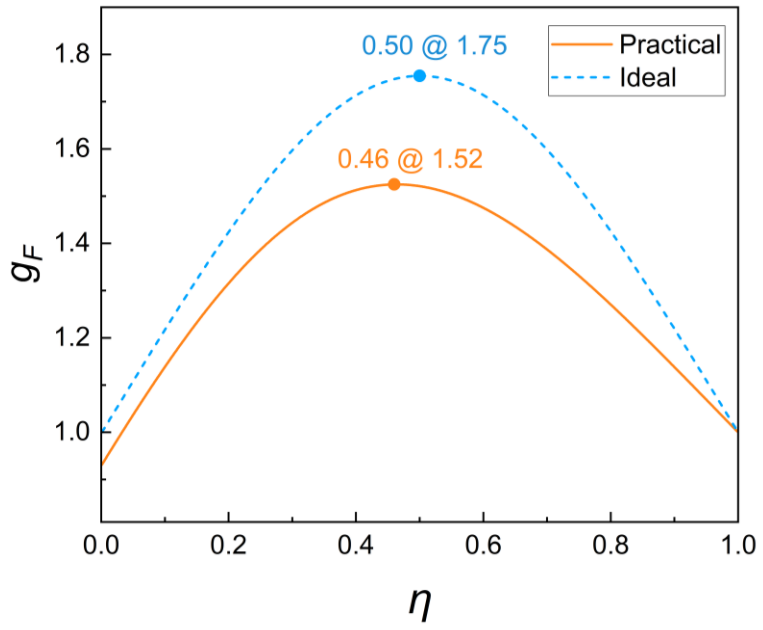


**Fig. S3** The relationship between the power ratio of $LP_{01}$ $\eta$ and $g_F$ (the contrast of MV-FPI and the contrast of single-mode FPI).

## Note 3. Theory of the SRC photoacoustic response

Based on the static bending theory of cantilever beams in material mechanics, the natural stiffness coefficient $k$ of a cantilever beam subjected to a concentrated force at its free end determined solely by the material properties and geometric dimensions of the cantilever itself, is given by:

$$k = \frac{Ewh^3}{4L_{eff}^3} \tag{S17}$$

where $E$ denotes the Young's modulus of the cantilever material, $w$ is the width of a single cantilever beam, $h$ is the thickness of the cantilever beam, and $L_{eff}$ is the effective length of a cantilever. Physically, the stiffness coefficient is proportional to the cube of the beam thickness and inversely proportional to the cube of the beam length: a longer length or thinner thickness leads to a smaller stiffness coefficient, which in turn contributes to a higher-pressure sensitivity of the sensor. Substituting the stiffness coefficient $k$ into the motion equation of the cantilever, the amplitude of the free-end displacement of the cantilever can be solved as:

$$\Delta L = \frac{p_0 A_{eff}}{m\sqrt{\left(\omega_0^2 - \omega^2\right)^2 + \left(\omega D / m\right)^2}} \tag{S18}$$

where $\omega_0 = \sqrt{k/m}$ is the fundamental natural resonant angular frequency of the cantilever beam, $m$ is the equivalent mass of the cantilever, $D$ is the damping coefficient, $P_0$ is the pressure of the amplified photoacoustic signal in the BHCF, and $A_{eff}$ is the effective area of the sound pressure equal to the core area of the BHCF. This research work is at the fundamental resonant frequency $\omega = \omega_0$, so:

$$\Delta L = \frac{p_0 A_{eff} / m}{\omega_0 D / m} = \frac{p_0 A_{eff}}{\omega_0 D} \tag{S19}$$

In mechanical vibration systems, the quality factor $Q = \omega_0 m / D$ is a core physical quantity that characterizes the damping level and the system's resonant amplification capability. Therefore, it can be further deduced as:

$$\omega_0 D = \frac{\omega_0^2 m}{Q} = \frac{k}{Q} \tag{S20}$$

Bringing Eq. (S19) into Eq. (S20), we can get:

$$\Delta L = \frac{p_0 A_{eff} Q}{k} \quad \text{S(21)}$$

The transient sound pressure generated by the photoacoustic effect is directly converted into dynamic changes in the FP cavity length through the elastic vibration of the square-ring cantilever (SRC) diaphragm. Under such conditions, the transient total length of the FP cavity can be expressed as:

$$L(t) = L_0 + \Delta L = L_0 + \frac{p_0 A_{eff} Q}{k} \quad \text{S(22)}$$

where $L_0$ is the initial static length of the FP cavity. The dynamic variation of the FP cavity length synchronously modulates the round-trip propagation phase shifts of the $LP_{01}$ and $LP_{11}$ modes. Substituting the transient cavity length $L(t)$ into the mode phase shift expression, the transient phase shifts of the two modes are obtained as follows:

$$\Delta\phi_{01} = \frac{4\pi}{\lambda_0} n_{01} \Delta L, \Delta\phi_{11} = \frac{4\pi}{\lambda_0} n_{11} \Delta L \quad \text{S(23)}$$

where $n_{11}$ and $n_{01}$ are the effective RIs of the $LP_{01}$ and $LP_{11}$ modes, respectively, and $\lambda_0$ is the wavelength of the pump light.

## Note 4. The MV-FPI acoustic signal measurement system

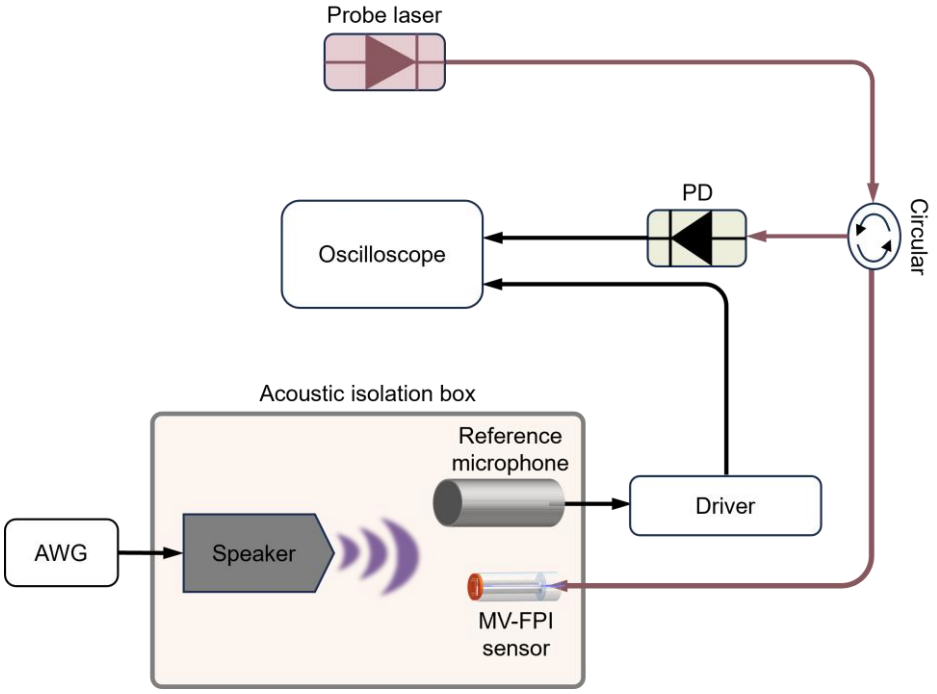


**Fig. S4.** Schematic of the acoustic response test setup for the MV-FPI sensor. The probe laser wavelength is 1532.3 nm. PD: photodetector; AWG: arbitrary waveform generator, output frequency range: 1 kHz–20 kHz.

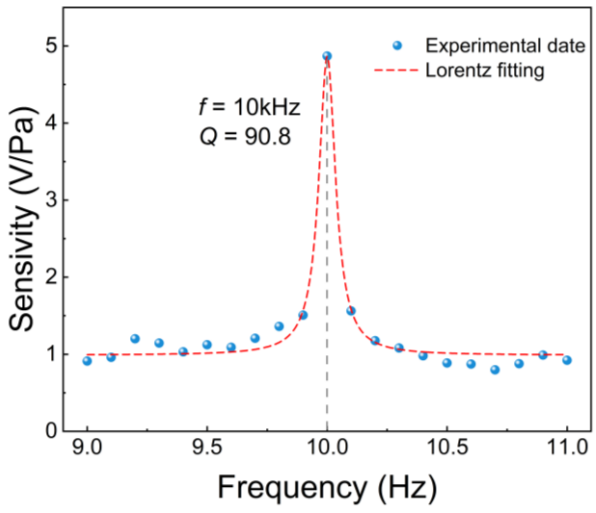


**Fig. S5.** Experimental measurement of the frequency response of the SRC around its resonant frequency of ~10 kHz, yielding a quality factor of approximately 90.8.

## Note 5. The length influence of the BHCF on the reflection spectrum of MV-FPI

In this work, by optimizing the fusion splicing process between the SMF and the BHCF, as well as the fabrication procedure of the SRC, we achieve precise control of the energy ratio between the two resonant modes. Meanwhile, a natural gas flow channel connected to the ambient environment is constructed using the pre-engineered gap in the SRC structure. When the incident light beam propagates to the SRC interface, a portion of the optical field is reflected into the BHCF for the excitation and detection of photoacoustic signals. In contrast, the remaining optical field is directly dissipated into free space. On this basis, the longitudinal height of the SRC should not be excessively large; otherwise, it will induce mode degradation of the transmitted beam, degrade it into free-space propagating light, and disrupt the optical field confinement of the waveguide. For this purpose, the nominal height of the SRC designed in this work is 10 μm, and a 5 μm-thick sacrificial layer is reserved during the two-photon polymerization (TPP) printing process, resulting in an actual height of approximately 5 μm for the as-fabricated SRC. At this dimension, the propagation effect of the light beam within the SRC can be negligibly small, and the optical field propagation is still predominantly governed by the anti-resonant reflecting optical waveguide (ARROW) mechanism of the BHCF.

As derived from Eq. (3), the photoacoustic phase is independent of the BHCF cavity length. Thus, the BHCF length does not directly affect the core performance of the MV-PAS system. Furthermore, as shown in Eq. (S16), the enhancement of the Vernier envelope signal $F_{env}$ is mainly determined by the energy ratio of the two modes, which is also independent of the BHCF length. Fig. S6a presents the measured reflection spectrum enhanced by the modal Vernier effect (MVE) for different BHCF lengths, showing that the interference spectrum contrast of the MV-FPI is significantly improved across all tested lengths. Considering that the central wavelength of the probe light employed in this work is located in the 1550 nm band, we comprehensively balance the requirement for device miniaturization and the operating band characteristics of the probe light, and finally select a BHCF with a length of 976 μm, whose reflection spectrum is shown in Fig. S6b. This device design offers excellent flexibility, and BHCFs of different lengths can be tailored to the requirements of practical application scenarios. The morphological characteristics of the fabricated sensor structure were characterized via optical microscopy and scanning electron microscopy, with the corresponding micrographs shown in Fig. S7.

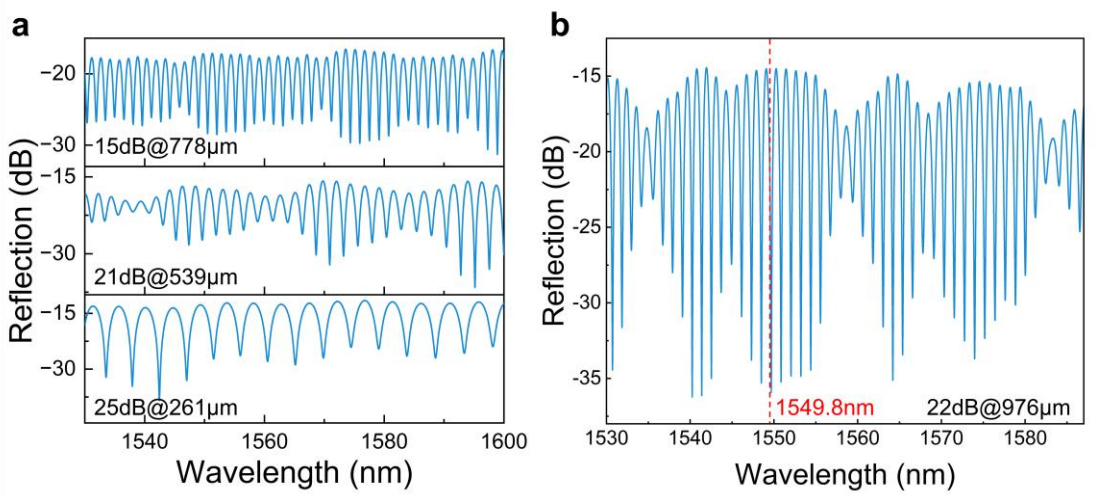


**Fig. S6 a** Measured reflection spectrum of the fabricated MV-PAS sensors based on BHCFs with varying lengths. **b** Reflection spectrum of the 976-μm-long BHCF structure, which exhibits high fringe contrast near the 1550 nm band and is adopted for gas detection experiments, with the probe wavelength fixed at 1549.8 nm.

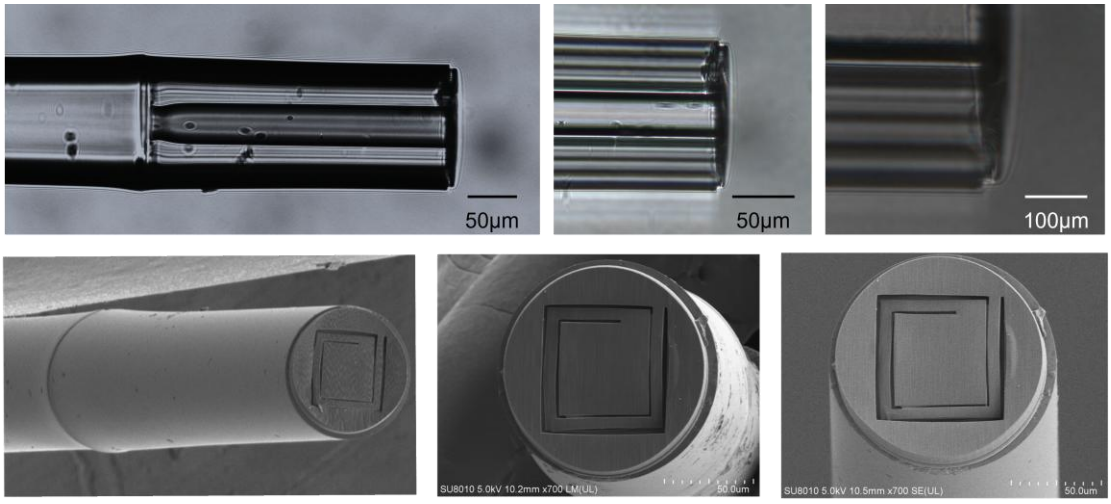


**Fig. S7** Optical microscopy and scanning electron microscopy micrographs of the fabricated MV-PAS gas sensor.

## Note 6. Performance comparison with other fiber microcavity gas sensors

**Table S1** Comparison of various fiber microcavity laser gas sensors

| Method | Pump power | Sensing unit | NEC | Dynamic range | Response time[s] |
|---|---|---|---|---|---|
| High finesse PTS[6] | 66 mW | 106 μm air cavity | 78 ppb $CH_4$@100s | $10^6$ | N.A. |
| Film PTS[7] | 384 mV | 348 μm air cavity | 213 ppb $C_2H_2$@220s | $10^5$ | N.A. |
| 3D-Microprinted PTS[8] | 396 mW | 66 μm air cavity | 160 ppb $C_2H_2$@433s | $10^6$ | ~ 0.5 |
| Spheric surface SMF PTS[9] | 1mW | 473 μm air cavity | 10 ppb $C_2H_2$@440s | $10^5$ | 1.7 |
| MV-PTS[4] | 196 mW | 1008 μm HCF | 12 ppb $C_2H_2$@303s | $10^6$ | ~ 3 |
| Fiber film PAS[5] | 50 mW | 60 μm HCF | 9 ppb $C_2H_2$@200s | $10^6$ | ~ 0.02 |
| OMR-PAS[10] | 210 mW | 84 μm air cavity | 55 ppb $C_2H_2$@356s | $10^5$ | ~ 0.2 |
| SMF-tip PAS[11] | 55 mW | 85 μm air cavity | 258ppb $C_2H_2$@100s | $10^5$ | ~ 0.028 |
| **This work** | **100 mW** | **976 μm HCF** | **567 ppt $C_2H_2$@297s** | **$10^8$** | **~ 1.3** |

## References


1. Xu, Y. et al. Asymptotic analysis of silicon based Bragg fibers. *Opt. Express* **11**(9): 1039-1049 (2003).
2. Xu, Y. et al. Asymptotic matrix theory of Bragg fibers. *J. Lightwave Technol.* **20**(3): 428-440 (2002).
3. Zhao, Z. et al. Sensitivity Amplification High Temperature Fiber Sensor Based on Bragg Hollow-Core Fiber and Harmonic Vernier Effect. *IEEE Sens. J.* **23**, 20 (2023).
4. Zhao, Z. et al. Microscale Intrinsic Fiber Mode Vernier Photothermal Spectroscopy Gas Sensing. *Laser & Photonics Rev.* **20**, 2: e02114 (2026).
5. Ma, J. et al. Microscale fiber photoacoustic spectroscopy for in situ and real-time trace gas sensing. *Adv. Photonics* **6**, 6 (2024).
6. Karol, K. et al. Photothermal gas detection using a miniaturized fiber Fabry-Perot cavity. *Sens. Actuators. B. Chem.* **401**, 135040 (2024).
7. Ran, S. et al. Fiber-tip photothermal transducer with gold-coated multi-beam interferometric cavity for high sensitivity gas detection. *Appl. Phys. Lett.* **126**, 6 (2025).
8. Zhao, P. et al. Ultraminiature Optical Fiber-Tip 3D-Microprinted Photothermal Interferometric Gas Sensors. *Laser & Photonics Rev.* **18**, 9: 2301285 (2024).
9. Yan, Y. et al. Nanoliter-Scale Light–Matter Interaction in a Fiber-Tip Cavity Enables Sensitive Photothermal Gas Detection. *Laser & Photonics Rev.* **18**, 12: 2400907 (2024).
10. Li, T. et al. Ultra-miniature and sensitive optical fiber-tip optomechanical resonant photoacoustic spectroscopy gas sensors. *Photoacoustics* **46**, 100784 (2025).
11. Fan, E. et al. Direct Laser Writing of Ultrathin and Scalable Optomechanical Membranes in Fiber-Tip Micro-Cavities for Multi-Gas Photoacoustic Spectroscopy. *Laser & Photonics Rev.* e01689 (2026).